



Preparation of microporous MoS₂@carbon nanospheres for the electrochemical detection of hydrogen peroxide

In Woo Cho^a, Seung Uk Son^b, MinHo Yang^{a,*}, Jaewon Choi^{c,*}

^a Department of Energy Engineering, Dankook University, Cheonan 31116, Republic of Korea

^b Department of Chemistry, Sungkyunkwan University, Suwon 16419, Republic of Korea

^c Department of Chemistry and Research Institute of Natural Science, Gyeongsang National University, Jinju 52828, Republic of Korea

ARTICLE INFO

Article history:

Received 25 August 2020

Received in revised form 29 September 2020

Accepted 30 September 2020

Available online 3 October 2020

Keywords:

Molybdenum disulfide

Microporosity

Composited nanosphere

Electrochemical sensor

Hydrogen peroxide

ABSTRACT

Molybdenum sulfide (MoS₂) may be a promising material for biosensing applications due to their remarkable electronic, electrochemical attributes, and luminescence properties. Herein, thin layered MoS₂ deposited on carbon nanospheres with microporosity (m-MoS₂@CNS) was prepared through a simple dip-calcination method. The as-prepared m-MoS₂@CNS exhibits the well-defined pore, high surface area, and good electrical conductivity, which lead to facilitated electron/ion transport during electrochemical reaction. Based on their outstanding electrochemical properties, the m-MoS₂@CNS reveals the excellent performance as a non-enzymatic detection of hydrogen peroxide in a wide concentration range, from 0.1 mM to 20 mM, with high sensitivity (8.89 μA/mM·cm²) and low limit of detection (7.5 μM, S/N = 3). Moreover, the electrode has a favorable selectivity, reproducibility, and fast response time (~7 s). Thus, the m-MoS₂@CNS has a great potential as an electrocatalyst for the efficient detection of hydrogen peroxide.

1. Introduction

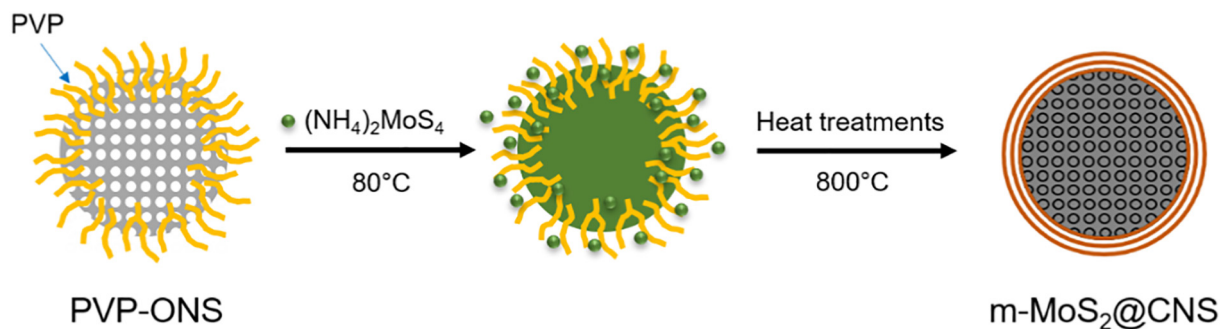
Hydrogen peroxide (H₂O₂) is an important molecule used as not only an oxidizing agent in various fields, such as pulp, cosmetics, food, and pharmaceutical industries but also a mediator in biological system [1–5]. In particular, abnormally high concentration of H₂O₂ in vivo induce the neuronal apoptosis, which can cause neurodegenerative diseases, such as Parkinson's, Alzheimer's, and multiple sclerosis [6–9]. Moreover, the H₂O₂-generated by enzyme-catalyzed reaction in vitro has been considered as one of the most valuable markers for analytical/clinical diagnostics [10]. Therefore, the precise detection and quantification of H₂O₂ are in great demand. Up to now, numerous techniques, such as colorimetric, luminescent, fluorescent, and electrochemical methods have been exploited [11–15]. Among them, electrochemical detection is one of the most convenient methods, which allows for rapid, accurate, and sensitive quantitation [16]. The H₂O₂ detection can be accomplished via enzymatic and nonenzymatic approaches [16]. Hydrogen peroxidase has been widely used as an enzymatic probe due to high activity and specificity towards H₂O₂ [17]. However, several drawbacks of enzyme-based approaches have been emerged in practical applications: i) reduced and loss of enzyme activity in harsh condition, ii) poor storage and operational stability, and iii) high

cost and time-consuming production. Nonenzymatic detection is based on catalytic nanomaterials that display peroxidase-like activity, which has drawn great attention due to the unique advantages over natural enzymes, such as low cost, scalable production, high stability, and tunable catalytic activity [18].

Layered transition metal dichalcogenides, such as MoS₂, MoSe₃, CuS, and VS₂, have been explored for highly sensitive biosensing due to their remarkable electronic and optical properties [19–22]. Among them, MoS₂ with a S-Mo-S layered sandwich structure has been extensively investigated as a promising electrode material for electrochemical biosensing of H₂O₂ [19,23]. However, its inferior electrical conductivity (<2.09 × 10⁻⁶ S/cm) and the limited active sites arising from multi-stacked layer of the MoS₂ are major drawbacks to adopted as an electrode towards practical applications [24]. A number of studies have been devoted to overcome these problems: i) tuning the atomic structures, ii) nanosizing, and iii) coupling with conductive agents [25–27]. In particular, direct anchoring of MoS₂ to nanocarbons, such as carbon dots, carbon nanotubes, and graphene improved the electrochemical performances due to excellent electrical contact and high loadings [28–30]. Nevertheless, it still a challenge to fabricate electrode with the tailored pore structures to ensure efficient ion transport in electrochemical process.

* Corresponding authors.

E-mail addresses: mhyang@dankook.ac.kr, (M. Yang), cjw0910@gnu.ac.kr, (J. Choi).



Scheme 1. Schematic illustration of the preparation of m-MoS₂@CNS.

In this work, we demonstrate the preparation of the microporous MoS₂ on carbon nanospheres (m-MoS₂@CNS) that ensure high performance of nonenzymatic electrochemical detection of H₂O₂. The thin layer of MoS₂ was formed on microporous carbon nanospheres via a simple dipping-calcination method. The well-defined pore system of m-MoS₂@CNS provides a large surface area and an efficient pathway for ion transport during electrochemical reactions. In addition, as-prepared m-MoS₂@CNS shows the excellent electrocatalytic activities towards H₂O₂, leading to high sensitivity over a wide linear range, selectivity, stability, and reproducibility.

2. Experimental section

2.1. Materials

Ammonium tetrathiomolybdate ((NH₄)₂MoS₄), uric acid (UA), dopamine hydrochloride (DA), and glucose were purchased from Sigma-Aldrich. Hydrogen peroxide (H₂O₂) and sodium hydroxide (NaOH) were obtained from Junsei. All chemicals were used as supplied without further purification.

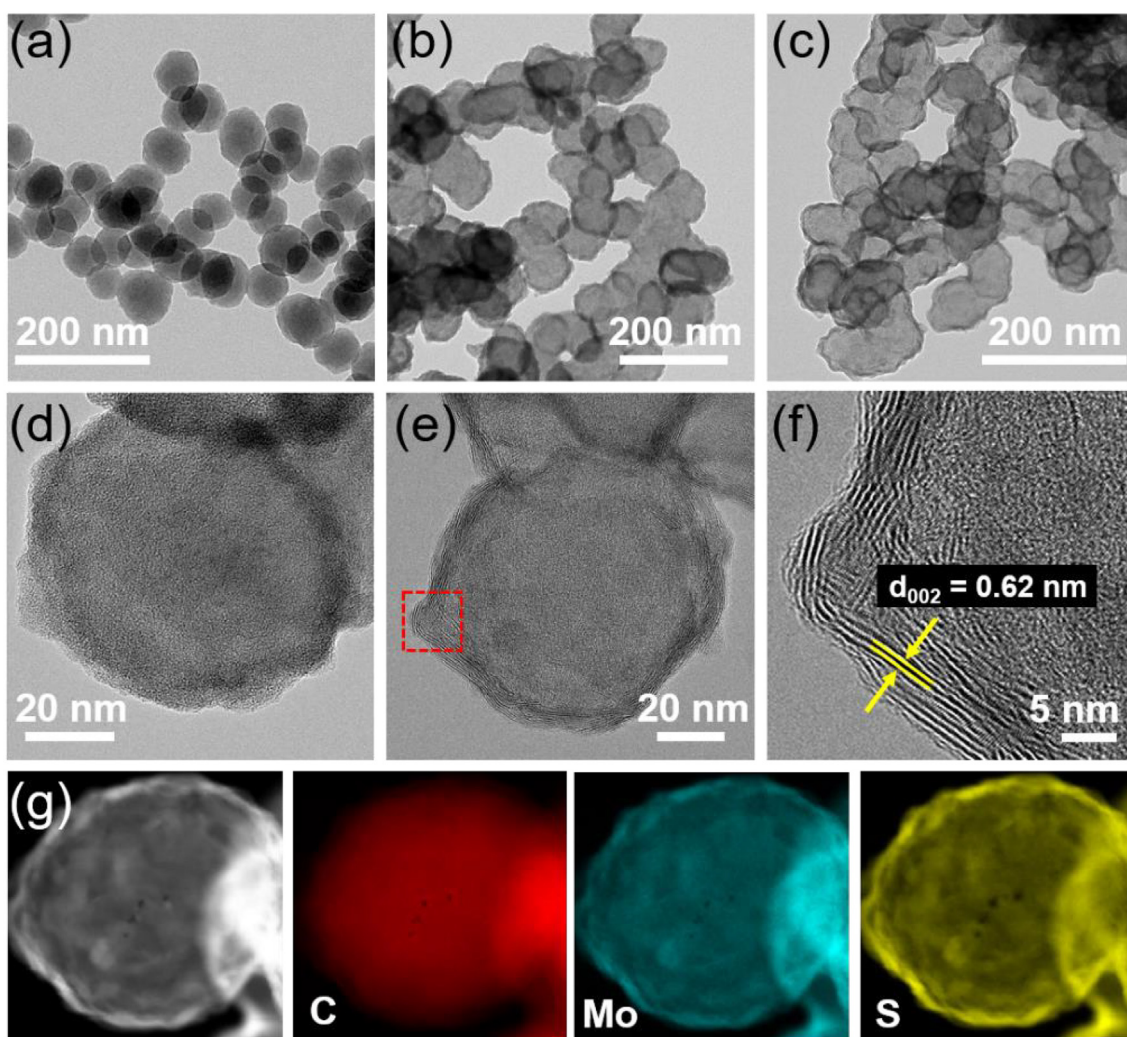


Fig. 1. TEM images of (a) PVP-ONS, (b) PVP-ONS after dipping in (NH₄)₂MoS₄ solution, and (c) m-MoS₂@CNS. HR-TEM images of (d) PVP-ONS after dipping in (NH₄)₂MoS₄ solution and (e and f) m-MoS₂@CNS; interlayer spacing is about 0.62 nm. (g) EELS elemental mapping of m-MoS₂@CNS.

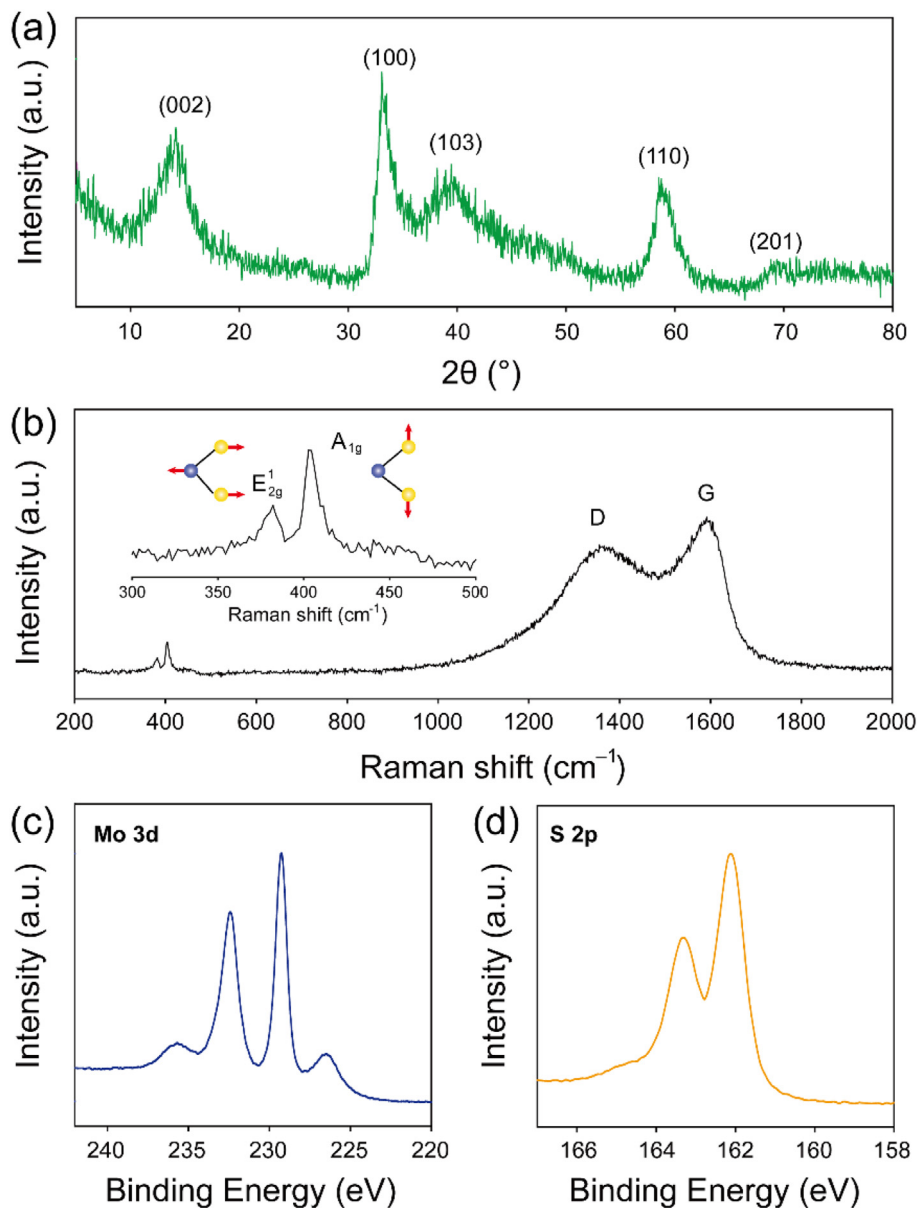


Fig. 2. (a) XRD pattern, (b) Raman spectra, (c and d) XPS spectra of Mo 3d and S 2p of the m-MoS₂@CNS, respectively.

2.2. Synthesis of m-MoS₂@CNS

The synthesis of m-MoS₂@CNS is presented in Scheme 1. First, the polyvinylpyrrolidone-entrapped organic nanospheres (PVP-ONS) were prepared as a template following the reported method [31]. Then, 50 mg of the PVP-ONS was sonicated in methanol (20 mL) for 1.5 h, mixed with 0.114 g of the (NH₄)₂MoS₄ (0.114 g), and heated at 80 °C overnight. Afterward, the excess (NH₄)₂MoS₄ was removed by centrifugation/wash/redispersion in methanol. The resultant solid was dried under vacuum for 12 h. Finally, the as-prepared powder was heated to 800 °C in inert Ar flow with a heating rate 5 °C/min and then held for 3 h. As-synthesized samples at each step was.

2.3. Electrode preparation

Prior to use, the glassy carbon electrode (GCE) was first polished with 0.05 μm alumina slurry and then washed several times with ethanol and de-ionized water. Three milligrams of as-prepared m-MoS₂@CNS were dispersed in 6 mL of ethanol and sonicated in water bath for 30 min to

obtain a homogenous dispersion. A 5 μL of final suspension was dropped onto the GCE and dried in air. Afterward, a 5 μL of Nafion solution (0.5 wt%) was drop cast onto the m-MoS₂@CNS modified GCE and dried under vacuum at room temperature.

2.4. Material and electrochemical characterization

Scanning electron microscopic (SEM) images were obtained using a JSM6700F. High resolution transmission electron microscopy (HR-TEM) and electron energy loss spectroscopy (EELS) images were collected using JEOL JEM 2100F. X-ray diffraction (XRD) pattern was recorded on Rigaku MAX-2200 diffractometer. X-ray photoelectron spectroscopy (XPS) investigation was performed on Thermo VG spectrometer with Al Kα X-ray source (1486.7 eV). The adsorption-desorption isotherm of N₂ were measured at 77 K using a BELSORP II-mini equipment and a Micromeritics ASAP2020. Raman spectra were obtained by Renishaw inVia™ Raman spectrometer. Electrochemical measurements were carried out using Bio-Logics SP-200 potentiostats at room temperature with three electrode system: a Pt wire as the counter electrode, an Ag/AgCl (3 M KCl) as the reference electrode,

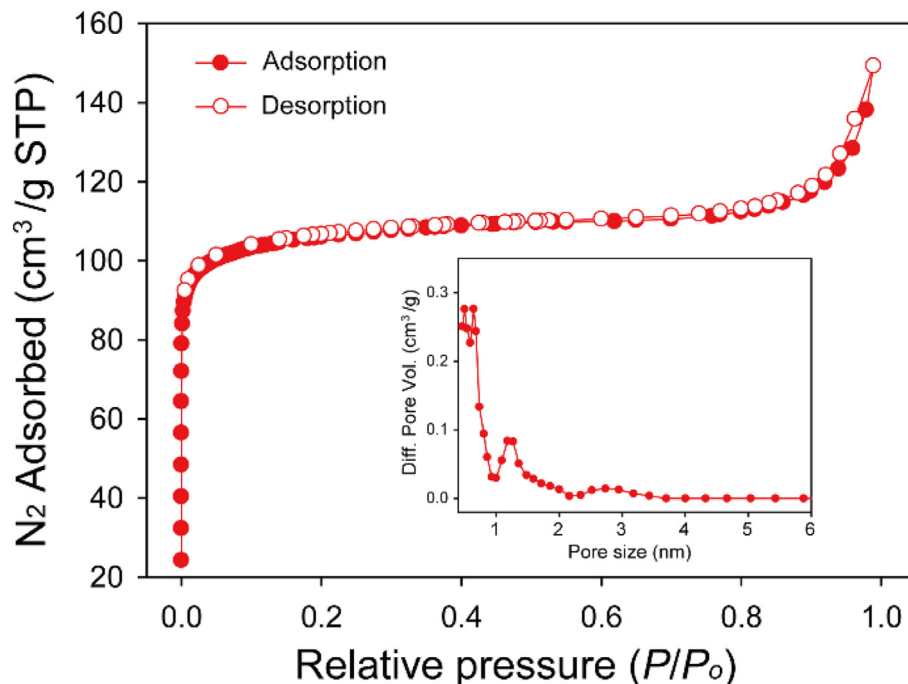


Fig. 3. BET N_2 adsorption-desorption isotherm of the m- $MoS_2@CNS$. Inset is corresponding pore size distribution.

and the modified GGE as the working electrode. AC impedance was performed in the range of 0.01 Hz to 100 kHz at disturbance potential of 10 mV.

3. Results and discussion

The ultra-thin layer of MoS_2 on carbon nanospheres with microporosity was prepared by the following steps: the PVP-entrapped organic nanospheres (ONS) as templates were firstly synthesized by the Sonogashira coupling of tetra(4-ethynylphenyl)methane and 1,4-diiodobenzene in presence of PVP. Representative TEM images of ONS shown in Fig. 1a confirmed that the ONS have uniform spherical shape with an average diameter of 82 nm. After immersion in $(NH_4)_2MoS_4$ solution, surface shell was formed due to trapping MoS_4^{2-} at the surface via ionic-dipole interaction between amine groups of PVP and MoS_4^{2-} (Fig. 1b and d). No lattice fringes can be observed in Fig. 1d, indicating that surface shell is amorphous. As shown in Fig. 1c and d, the entrapped MoS_4^{2-} onto ONS led to formation of MoS_2 thin layer on carbon nanospheres (CNS) by heat treatment. The HR-TEM images confirmed that thin layer of MoS_2 not only was 4–6 nm in thickness and but also has lattice spacing of 0.62 nm corresponding to (002) plane of crystalline MoS_2 (Fig. 1e and f) [32]. The PVP-ONS, PVP-ONS immersed in $(NH_4)_2MoS_4$ solution, and m- $MoS_2@CNS$ samples were also observed by SEM, which shows the uniform spherical shapes with slight aggregation (Fig. S1). Elemental mapping of m- $MoS_2@CNS$ in Fig. 1g reveals Mo, S, and C elements were located across entire area of the particles. Interestingly, both Mo and S intensities are higher at the edge of spheres, which verifies conformal coating of MoS_2 on the surface of CNS.

The crystal structure and chemical composition of the as-obtained product were characterized by powder XRD, Raman, and XPS measurements. Fig. 2a shows the XRD pattern of the as-prepared m- $MoS_2@CNS$. The broad diffraction peaks located at 14.3, 33.1, 38.3, and 58.3° can be well indexed to the (002), (100), (103), and (110) planes of hexagonal MoS_2 , respectively (JCPDS: 37–1492) [32]. Moreover, the presence of the broad diffraction peaks between 20 and 30° suggests the carbon in m- $MoS_2@CNS$ should be amorphous owing to low annealing temperature. Fig. 2b represents the Raman spectrum of m- $MoS_2@CNS$. Two peaks at 382 and 403 cm^{-1} can be observed, which correspond to opposite vibration of

two S atoms against Mo atoms and out of plane vibration of only S atoms, respectively [33]. Besides, the two additional broad peaks are observed at 1360 and 1592 cm^{-1} , attributed to D-band and G-band of carbon content in as-prepared composites [34]. The I_D/I_G ratio was estimated to be 0.83, indicating that a mixture of sp^2 and sp^3 carbon was formed during carbonization at given temperature. To further obtain the compositional information of m- $MoS_2@CNS$, XPS measurements were conducted. In Fig. 2c, the high resolution XPS spectrum of Mo 3d reveals the two major peaks at 232.3 and 229.2 eV, attributed to the $Mo^{4+} 3d_{3/2}$ and $Mo^{4+} 3d_{5/2}$, respectively, in MoS_2 [35]. Besides the Mo^{4+} signal, the additional peak observed around 236 eV corresponds to $Mo^{6+} 3d_{3/2}$ due to amorphous MoO_3 species derived from the exposure of the samples to air. High resolution XPS spectrum of S 2p shows the peaks at 163.2 and 162.0 eV, assigned to S 2p_{1/2} and S 2p_{3/2}, respectively, indicating –2 oxidation state of sulfur in MoS_2 [35].

N_2 adsorption-desorption isotherm at 77 K was performed to characterize the textural properties of the as-prepared m- $MoS_2@CNS$. Fig. 3 shows the typical adsorption-desorption isotherm of m- $MoS_2@CNS$. N_2 adsorption content rapidly increases at low relative pressure (below 0.02), indicating structured with micropores (Type I) [36]. Also, the BET surface area of m- $MoS_2@CNS$ reaches up to 420.3 m^2/g . It results from the formation of microporous network during carbonization of $(NH_4)_2MoS_4@ONS$. The pore size distribution of the samples was also calculated by the density functional theory. As shown in inset of Fig. 3, the m- $MoS_2@CNS$ represent narrow micropore distribution with an average pore size of 2.20 nm. Thus, m- $MoS_2@CNS$ with large surface area can be expected to significantly as promising materials for electrochemical applications where electron and ion transport is dominant.

The electrochemical properties of the m- $MoS_2@CNS$ and c- MoS_2 was investigated by CV and EIS measurements in 5 mM $[Fe(CN)_6]^{3-/4-}$ solution. As shown in Fig. 4a, a pair of redox couple of $[Fe(CN)_6]^{3-/4-}$ are observed at both electrodes. Interestingly, the m- $MoS_2@CNS$ reveals dramatic increases in peak currents and significant decreases in peak to peak separation, comparing with the c- MoS_2 electrode. This result indicates that the m- $MoS_2@CNS$ allows for the facilitated electron transfer and improved accessibility of ions, arising from conductive carbon matrix, well-defined pores, and large surface area. Fig. 4b represents CV curves of m- $MoS_2@CNS$ measured at different scan rates from 2 to 50 mV/s. It is clearly observed that peak currents increase along with the scan rates. Moreover, a linear relationship

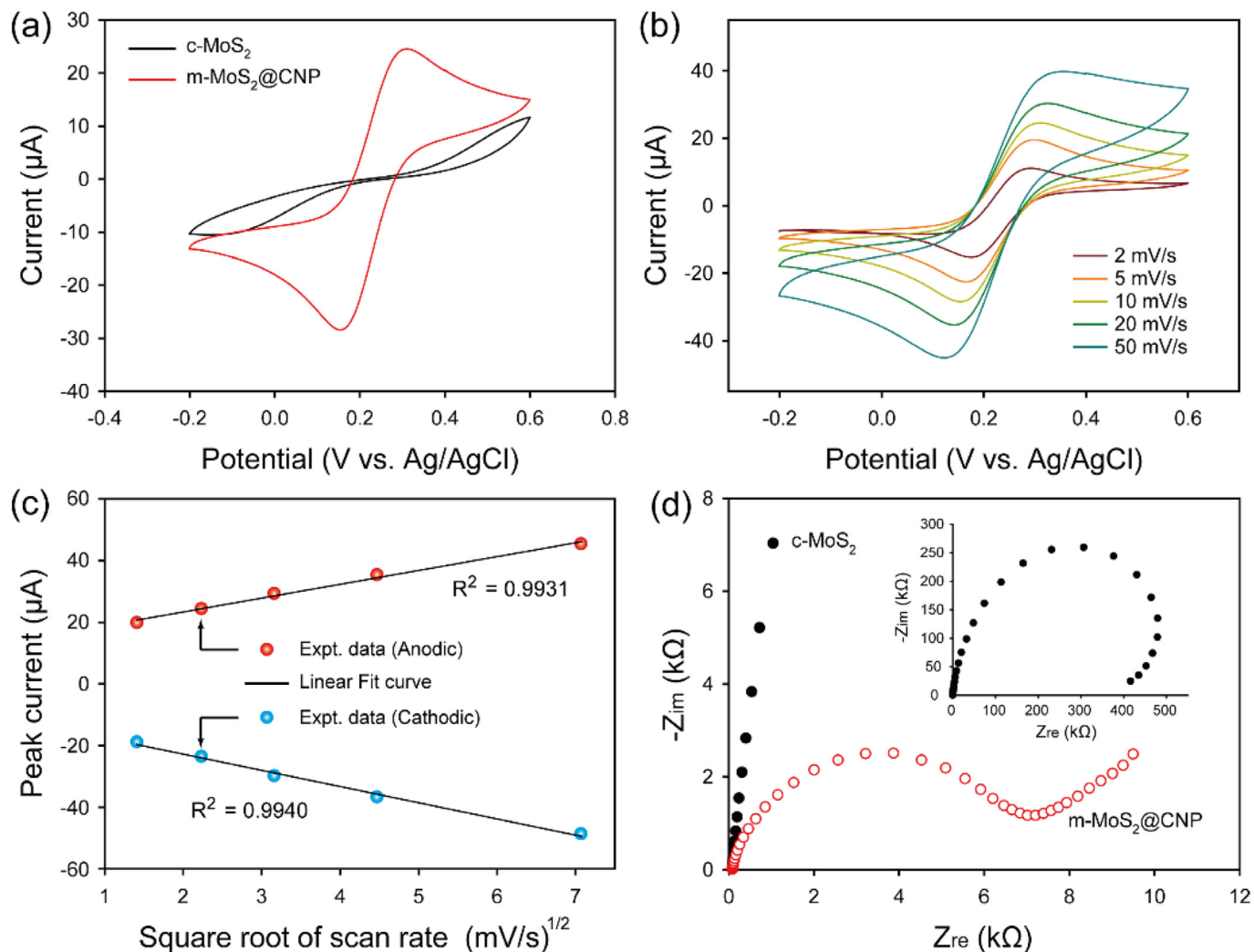


Fig. 4. CV curves of the electrodes based on (a) c-MoS₂ and m-MoS₂@CNS at 20 mV/s and (b) m-MoS₂@CNS at various scan rate from 2 to 50 mV/s in 5 mM [Fe(CN)₆]^{3-/-4-} containing 0.1 M KCl. (c) Plot of redox peak current of m-MoS₂@CNS electrode vs. square root of scan rate. (d) Nyquist plot of c-MoS₂ and m-MoS₂@CNS electrodes.

between peak currents and square root of scan rates are obtained (Fig. 4c), indicating diffusion-controlled electrochemical process with fast electron transfer [37]. Fig. 4d shows the Nyquist plot of m-MoS₂@CNS and c-MoS₂ electrode. The semicircle diameter of the EIS curves was used to estimate the charge transfer resistance (R_{ct}) of electrodes. The R_{ct} value of m-MoS₂@CNS was 6.6 k Ω , much lower than that of c-MoS₂ (501 k Ω). The improved charge transfer of electrode might be due to unique architecture and good conductivity of the m-MoS₂@CNS, similar to the results obtained from CV.

The electrocatalytic activity of m-MoS₂@CNS towards H₂O₂ was evaluated by using three electrode system in N₂-saturated 0.1 M NaOH electrolyte at the scan rate of 20 mV/s. Fig. 5 represents typical CV curves of m-MoS₂@CNS and c-MoS₂ with 0.1 mM H₂O₂. The m-MoS₂@CNS exhibits the strong cathodic response (2.7 mA) at -0.37 V, which is ~2 times higher than that of c-MoS₂ in presence of H₂O₂. It indicates that the m-MoS₂@CNS has a better catalytic activity towards H₂O₂ due to a facilitated ion/electron transport originated from microporosity and good conductivity. In addition, cathodic current of m-MoS₂@CNS increases as increasing H₂O₂ concentration ranging from 0 to 0.7 mM (Fig. 5b). From this result, m-MoS₂@CNS can be employed as an amperometric sensing platform without enzymes (i.e., HRP) for precise and accurate detection of H₂O₂.

Fig. 6a reveals the amperometric response of m-MoS₂@CNS recorded at -0.35 V in 0.1 M NaOH with successive addition of H₂O₂. As shown, the cathodic current rapidly increases with addition of H₂O₂ and reaches the steady-state within 7 s. The linear responses with a slope of -0.628 (R² = 0.998) and -0.394 μ A/mM (R² = 0.995) were observed at concentration range from 0.1 to 1 mM and from 2 to 20 mM, respectively (Fig. 6b). From the slope of the calibration curve at low concentration, the sensitivity and limit of detection (S/N = 3) were calculated to be 8.89 μ A/mM \cdot cm² and 7.5 μ M, which are comparable values to other reported nonenzymatic H₂O₂ sensors (Table 1). In addition, the selectivity, one of significant figures of merit, was testified by addition of several potential interfering species, such as ascorbic acid (AA), uric acid (AA) and glucose. As shown in Fig. 6c, the amperometric response was negligibly changed after injection of interfering species while the cathodic current sharply increases with addition of H₂O₂. It indicates that the electrochemical sensor based on m-MoS₂@CNS has a good anti-interference and a high selectivity. In order to evaluate the reproducibility of m-MoS₂@CNS, the amperometric response for 2 mM H₂O₂ was recorded and the corresponding results was depicted in Fig. 6d. The relative standard deviation (RSD) obtained from the five individual electrodes is 2.5%, indicating an excellent reproducibility for detection of H₂O₂.

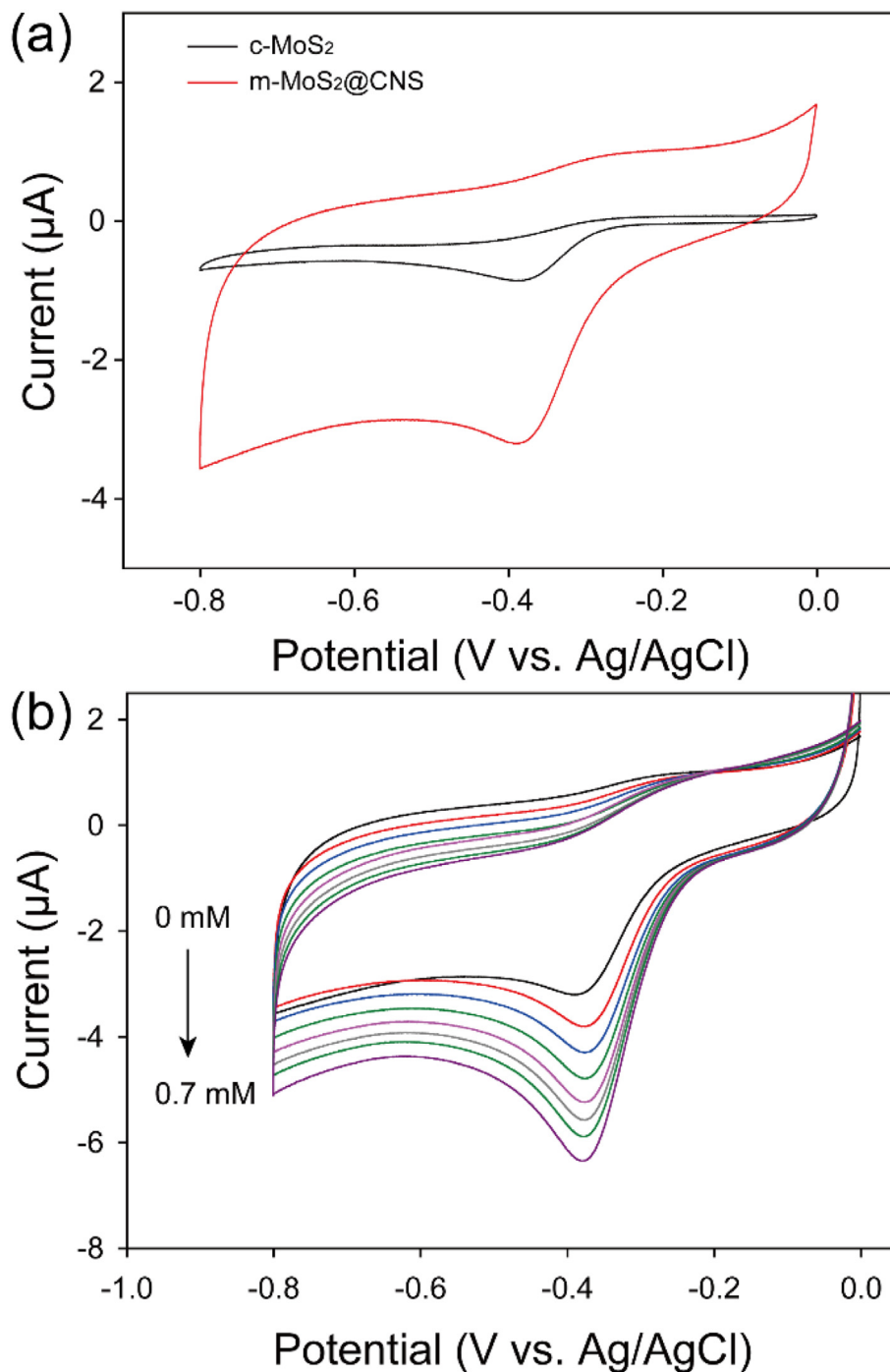


Fig. 5. CV curves of (a) c-MoS₂ and m-MoS₂@CNS electrodes in N₂-saturated 0.1 M NaOH containing 0.1 mM H₂O₂ at scan rate of 20 mV/s. (b) CV curves of m-MoS₂@CNS electrode with different concentration of H₂O₂ at 20 mV/s.

4. Conclusion

The m-MoS₂@CNS with unique morphology, high surface area, and excellent catalytic activity has been successively prepared via a simple dip-calcination procedure with a colloidal template (i.e., microporous carbon nanospheres). The intrinsic microporosity of templates plays a key role in entrapment of MoS₂ precursor ions, leading to formation of m-MoS₂@CNS with well-defined pore system after heat treatment. As-prepared m-MoS₂@CNS exhibited the improved electrochemical properties and

nonenzymatic electrocatalytic activities towards H₂O₂ with high sensitivity (8.89 μA/mM·cm²) over a wide linear range, low detection limit (7.5 μM), and superior selectivity. In addition, the m-MoS₂@CNS revealed the excellent stability and reproducibility with RSD of around 2.5%. The high performance of m-MoS₂@CNS is attributed to a large accessible surface area originated from their microporous structures and to efficient and fast ion/electron transfer during electrochemical reactions. Electrochemically active accessible area of ions and the facilitated ion/electron transport.

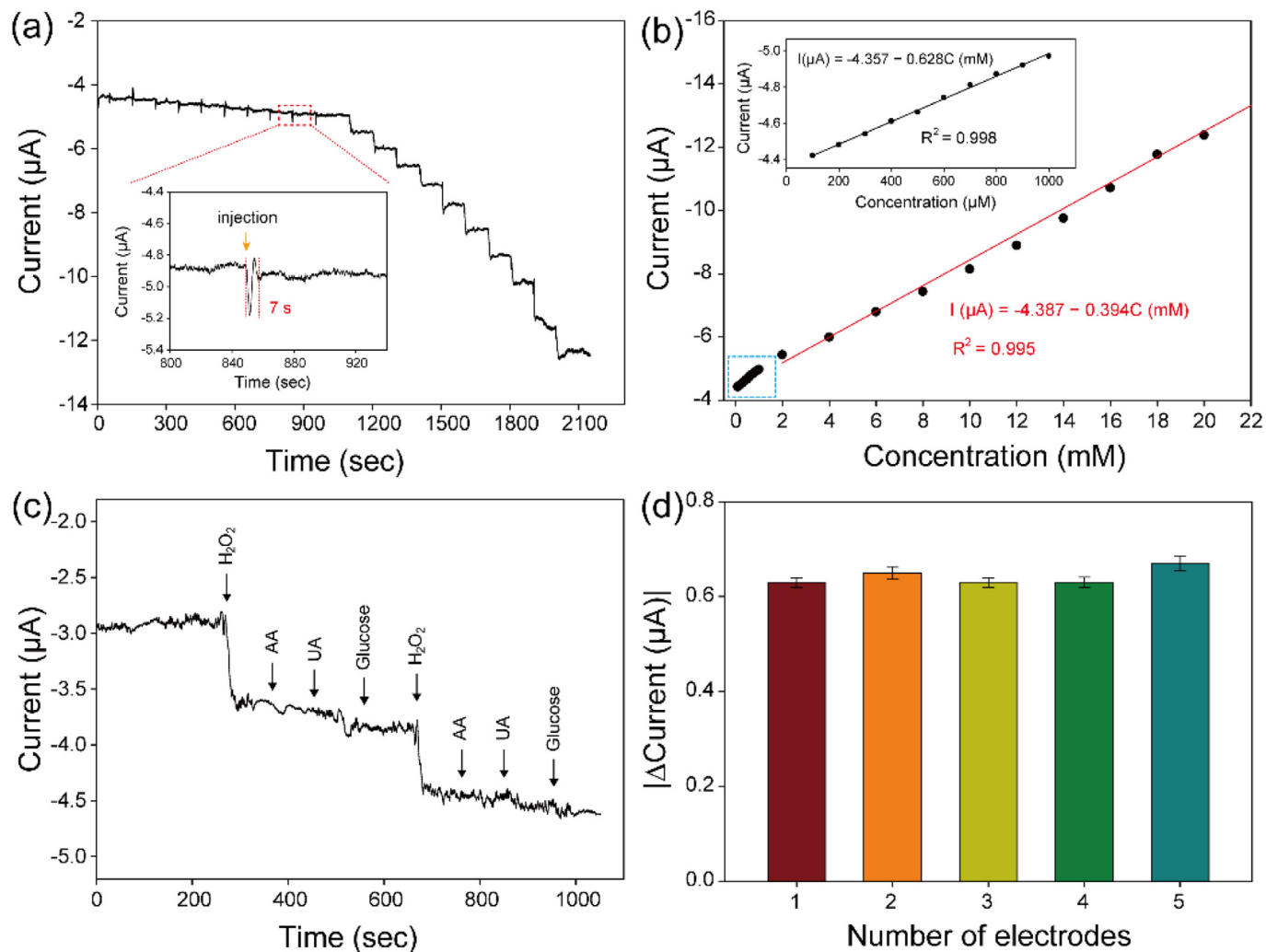


Fig. 6. (a) Amperometric response of m-MoS₂@CNS electrode in N₂-saturated 0.1 M NaOH at an applied potential of -0.35 V with successive addition of H₂O₂. (b) The corresponding calibration curve for H₂O₂ obtained at the m-MoS₂@CNS electrode. (c) Amperometric response of m-MoS₂@CNS electrode after successive addition of 1 mM H₂O₂ and 1 mM ascorbic acid (AA), uric acid (UA), and glucose. (d) Response current of five different m-MoS₂@CNS electrode with addition of 1 mM H₂O₂.

Table 1

Comparison of analytical performance of various nonenzymatic H₂O₂ sensors.

Electrode	Sensitivity (µA/mM·cm ²)	Limit of detection (µM)	Linear range (mM)	References
α-Fe ₂ O ₃	7.16	10	0.1–5.5	[38]
Ag/FeOOH	8.07	22.8	0.03–1.5	[39]
Ag/MoS ₂	54.5	3.5	0.025–135.2	[40]
Ag NW array	0.132	109	0.5–9.9	[41]
H ₃ PMo ₁₂ O ₄₀ /PANI nanopillar	6.3	8.1	0.1–10	[42]
MoS ₂ -ICPC	–	11.8	0.02–0.3	[43]
m-MoS ₂ @CNS	8.89	7.5	0.1–1.0	This work
	5.57	11.7	2–20	

NW: nanowire, PANI: polyaniline, ICPC: interconnected porous carbon heterostructure.

Declaration of Competing Interest

The authors declare that they have no known competing financial interests or personal relationships that could have appeared to influence the work reported in this paper.

Acknowledgment

The present research was conducted by the research fund of Dankook University in 2018.

Appendix A. Supplementary data

Supplementary data to this article can be found online at <https://doi.org/10.1016/j.jelechem.2020.114739>.

References

- [1] S.I. Mussatto, G.J.M. Rocha, I.C. Roberto, Hydrogen peroxide bleaching of cellulose pulps obtained from brewer's spent grain, *Cellulose* 15 (2008) 641–649, <https://doi.org/10.1007/s10570-008-9198-4>.
- [2] K.-H. Back, J.-W. Ha, D.-H. Kang, Effect of hydrogen peroxide vapor treatment for inactivating *Salmonella Typhimurium*, *Escherichia coli O157:H7* and *Listeria monocytogenes* on organic fresh lettuce, *Food Control* 44 (2014) 78–85, <https://doi.org/10.1016/j.foodcont.2014.03.046>.
- [3] O.J.X. Morel, R.M. Christie, Current trends in the chemistry of permanent hair dyeing, *Chem. Rev.* 111 (2011) 2537–2561, <https://doi.org/10.1021/cr1000145>.
- [4] C.J. Tredwin, S. Naik, N.J. Lewis, C. Scully, Hydrogen peroxide tooth-whitening (bleaching) products: review of adverse effects and safety issues, *Br. Den. J.* 200 (2006) 371–376, <https://doi.org/10.1038/sj.bdj.4813423>.

- [5] C.C. Winterbourn, Chapter one - the biological chemistry of hydrogen peroxide, *Methods Enzymol.* 528 (2013) 325, <https://doi.org/10.1016/B978-0-12-405881-1.00001-X>.
- [6] M.T. Lin, M.F. Beal, Mitochondrial dysfunction and oxidative stress in neurodegenerative diseases, *Nature* 443 (2006) 787–795, <https://doi.org/10.1038/nature05292>.
- [7] D. Pramanik, S.G. Dey, Active site environment of heme-bound amyloid β peptide associated with Alzheimer's disease, *J. Am. Chem. Soc.* 133 (2011) 81–87, <https://doi.org/10.1021/ja1084578>.
- [8] E.A. Mazzi, K.F.A. Soliman, Glioma cell antioxidant capacity relative to reactive oxygen species produced by dopamine, *J. Appl. Toxicol.* 24 (2004) 99–106, <https://doi.org/10.1002/jat.954>.
- [9] D.-H. Lee, R. Gold, R.A. Linker, Mechanisms of oxidative damage in multiple sclerosis and neurodegenerative diseases: therapeutic modulation via fumaric acid esters, *Int. J. Mol. Sci.* 13 (2012) 11783–11803, <https://doi.org/10.3390/ijms130911783>.
- [10] N. Adányi, T. Barna, T. Emri, M. Miskei, I. Pócsi, Hydrogen peroxide producing and decomposing enzymes: Their use in biosensors and other applications, in: J. Polaina, A.P. MacCabe (Eds.), *Industrial Enzymes*, Springer, Dordrecht 2007, pp. 441–459, https://doi.org/10.1007/1-4020-5377-0_25.
- [11] H. Liu, B. Ding, Z. Liu Yang, X. Zhang, Q. Liu, Iron doped $\text{CuSn}(\text{OH})_6$ microspheres as a peroxidase-mimicking artificial enzyme for H_2O_2 colorimetric detection, *ACS Sustainable Chem. Eng.* 6 (2018) 14383–14393, <https://doi.org/10.1021/acssuschemeng.8b03082>.
- [12] D.F. Henning, P. Merkl, C. Yun, F. Iovino, L. Xie, E. Mouzourakis, C. Moularas, Y. Deligiannakis, B. Henriques-Normark, K. Leifer, G.A. Sotiriou, Luminescent $\text{CeO}_2:\text{Eu}^{3+}$ nanocrystals for robust *in situ* H_2O_2 real-time detection in bacterial cell cultures, *Biosens. Bioelectron.* 132 (2019) 286–293, <https://doi.org/10.1016/j.bios.2019.03.012>.
- [13] J. Lee, S.A. Yoon, J. Chun, C. Kang, M.H. Lee, A red-emitting styrylnaphthalimide-based fluorescent probe providing a ratiometric signal change for the precise and quantitative detection of H_2O_2 , *Anal. Chim. Acta* 1080 (2019) 153–161, <https://doi.org/10.1016/j.aca.2019.07.008>.
- [14] M. Peng, T. Zhao, D. Chen, Y. Tan, T. Zhang, Free-standing 3D electrodes for electrochemical detection of hydrogen peroxide, *ChemCatChem* 11 (2019) 4222–4237, <https://doi.org/10.1002/cctc.201900913>.
- [15] C. Wang, S. Hung, L. Luo, Y. Zhou, X. Lu, G. Zhang, H. Ye, J. Gu, F. Cao, Ultrathin two-dimensional metal-organic framework nanosheets/multi-walled carbon nanotube composite films for the electrochemical detection of H_2O_2 , *J. Electroanal. Chem.* 835 (2019) 178–185, <https://doi.org/10.1016/j.jelechem.2019.01.030>.
- [16] N.J. Ronkainen, H.B. Halsall, W.R. Heineman, Electrochemical biosensors, *Chem. Soc. Rev.* 39 (2010) 1747–1763, <https://doi.org/10.1039/b714449k>.
- [17] M. Ali, M.N. Tahir, Z. Siwy, R. Neumann, W. Tremel, W. Ensinger, Hydrogen peroxide sensing with horseradish peroxidase-modified polymer single conical nanochannels, *ACS Nano* 5 (2011) 1673–1680, <https://doi.org/10.1021/ac102795a>.
- [18] X. Chen, G. Wu, Z. Cai, M. Oyama, X. Chen, Advances in enzyme-free electrochemical sensors for hydrogen peroxide, glucose, and uric acid, *Microchim. Acta* 181 (2014) 689–705, <https://doi.org/10.1007/s00604-013-1098-0>.
- [19] Y.-H. Wang, K.-J. Huang, X. Wu, Recent advances in transition-metal dichalcogenides based electrochemical biosensors: a review, *Biosens. Bioelectron.* 97 (2017) 305–316, <https://doi.org/10.1016/j.bios.2017.06.011>.
- [20] X. Wu, T. Chen, J. Wang, G. Yang, Few-layered MoSe_2 nanosheets as an efficient peroxidase nanozyme for highly sensitive colorimetric detection of H_2O_2 and xanthine, *J. Mater. Chem. B* 6 (2018) 105–111, <https://doi.org/10.1039/c7tb02434g>.
- [21] S. Zhang, B. Li, Q. Sheng, J. Zheng, Electrochemical sensor for sensitive determination of nitrite based on the CuS-MWCNT nanocomposites, *J. Electroanal. Chem.* 769 (2016) 118–123, <https://doi.org/10.1016/j.jelechem.2016.03.025>.
- [22] H. Yuan, J. Zhao, Q. Wang, D. Manoj, A. Zhao, K. Chi, J. Ren, W. He, Y. Zhang, Y. Sun, F. Xiao, S. Wang, Hierarchical core-shell structure of $2\text{D VS}_2@\text{VC}$ on N-doped carbon sheets decorated by ultrafine Pd nanoparticles: Assembled in a 3D rosette-like array on carbon fiber microelectrode for electrochemical sensing, *J. Electroanal. Chem.* 835 (2020) 15507–15516, <https://doi.org/10.1021/acsami.9b21436>.
- [23] T. Wang, H. Zhu, J. Zhuo, Z. Zhu, P. Papakonstantinou, G. Lubarsky, J. Lin, M. Li, Biosensor based on ultrasmall MoS_2 nanoparticles for electrochemical detection of H_2O_2 released by cells at the nanomolar level, *Anal. Chem.* 85 (2013) 10289–10295, <https://doi.org/10.1021/ac402114c>.
- [24] J.-M. Jeong, M. Yang, D.S. Kim, T.J. Lee, B.G. Choi, D.H. Kim, High performance electrochemical glucose sensor based on three-dimensional $\text{MoS}_2/\text{graphene}$ aerogel, *J. Colloid Interface Sci.* 506 (2017) 379–385, <https://doi.org/10.1016/j.jcis.2017.07.061>.
- [25] Y. Lei, D. Butler, M.C. Lucking, F. Zhang, T. Xia, K. Fujisawa, T. Granzier-Nakajima, R. Cruz-Silva, M. Endo, H. Terrones, M. Terrones, A. Ebrahimi, Single-atom doping of MoS_2 with manganese enables ultrasensitive detection of dopamine: Experimental and computational approach, *Sci. Adv.* 6 (2020) eabc4250, <https://doi.org/10.1126/sciadv.abc4250>.
- [26] S. Barua, H.S. Dutta, S. Gogoi, R. Devi, R. Khan, Nanostructured MoS_2 -based advanced biosensors: a review, *ACS Appl. Nano Mater.* 1 (2018) 2–25, <https://doi.org/10.1021/acsnm.7b00157>.
- [27] Y. Shu, J. Chen, Q. Xu, Z. Wei, F. Liu, R. Lu, S. Xu, X. Hu, MoS_2 nanosheet–Au nanorod hybrids for highly sensitive amperometric detection of H_2O_2 in living cells, *J. Mater. Chem. B* 5 (2017) 1446–1453, <https://doi.org/10.1039/c6tb02886a>.
- [28] I. Vasilescu, S.A.V. Eremia, M. Kusko, A. Radoi, E. Vasile, G.-L. Radu, Molybdenum disulfide and graphene quantum dots as electrode modifiers for laccase biosensor, *Biosens. Bioelectron.* 75 (2016) 232–237, <https://doi.org/10.1016/j.bios.2015.08.051>.
- [29] Y. Lin, X. Chen, Y. Lin, Q. Zhou, D. Tang, Non-enzymatic sensing of hydrogen peroxide using a glassy carbon electrode modified with a nanocomposite made from carbon nanotubes and molybdenum disulfide, *Microchim. Acta* 182 (2015) 1803–1809, <https://doi.org/10.1007/s00604-015-1517-5>.
- [30] F. Chekin, F. Teodorescu, Y. Coffinier, G.H. Pan, A. Barras, R. Boukherroub, S. Szunerits, $\text{MoS}_2/\text{reduced}$ graphene oxide as active hybrid material for the electrochemical detection of folic acid in human serum, *Biosens. Bioelectron.* 85 (2016) 807–813, <https://doi.org/10.1016/j.bios.2016.05.095>.
- [31] S.Y. Kang, C.W. Kang, D.W. Kim, Y. Myung, J. Choi, S.M. Lee, H.J. Kim, Y.-J. Ko, S.U. Son, Colloidal template synthesis of nanomaterials by using microporous organic nanoparticles: the case of $\text{C}@\text{MoS}_2$ nanoadsorbents, *Chem. Asian J.* 14 (2019) 3173–3180, <https://doi.org/10.1002/asia.201900885>.
- [32] L. Yang, X. Cui, J. Zhang, K. Wang, M. Shen, S. Zeng, S.A. Dayeh, L. Feng, B. Xiang, Lattice strain effects on the optical properties of MoS_2 nanosheets, *Sci. Rep.* 4 (2014) 5649, <https://doi.org/10.1038/srep05649>.
- [33] H. Li, Q. Zhang, C.C.R. Yap, B.K. Tay, T.H.T. Edwin, A. Olivier, D. Baillargeat, From bulk to monolayer MoS_2 : evolution of raman scattering, *Adv. Funct. Mater.* 22 (2012) 1385–1390, <https://doi.org/10.1002/adfm.201102111>.
- [34] M. Commodore, P.H. Joo, G.D. Falco, P. Minutolo, A. D'Anna, Ö.L. Cüldür, Raman spectroscopy of soot sampled in high-pressure diffusion flames, *Energy Fuel* 31 (2017) 10158–10164, <https://doi.org/10.1021/acs.energyfuels.7b01674>.
- [35] G. Chen, S. Wang, R. Yi, L. Tan, H. Li, M. Zhou, L. Yan, Y. Jiang, S. Tan, D. Wang, S. Deng, X. Meng, H. Luo, Facile synthesis of hierarchical MoS_2 -carbon microspheres as a robust anode for lithium ion batteries, *J. Mater. Chem. A* 4 (2016) 9653–9660, <https://doi.org/10.1039/c6ta03310e>.
- [36] K.S.W. Sing, D.H. Everett, R.A.W. Haul, L. Moscou, R.A. Pierotti, J. Rouquéro, T. Siemieniowska, Reporting physisorption data for gas/solid systems with special reference to the determination of surface area and porosity, *Pure Appl. Chem.* 57 (1985) 603–619, <https://doi.org/10.1351/pac198557040603>.
- [37] A.J. Bard, L.R. Faulkner, *Electrochemical Methods: Fundamentals and Applications*, Wiley, New York, 2001.
- [38] S. Majumder, B. Saha, S. Dey, R. Mondal, S. Kumar, S. Banerjee, A highly sensitive non-enzymatic hydrogen peroxide and hydrazine electrochemical sensor based on 3D micro-snowflake architectures of $\alpha\text{-Fe}_2\text{O}_3$, *RSC Adv.* 6 (2016) 59907–59918, <https://doi.org/10.1039/C6RA10470C>.
- [39] J. Zhang, J. Zheng, An enzyme-free hydrogen peroxide sensor based on Ag/FeOOH nanocomposites, *Anal. Methods* 7 (2015) 1788–1793, <https://doi.org/10.1039/C4AY02881C>.
- [40] Z. Zhao, J. Liu, W. Wang, J. Zhang, G. Li, J. Liu, K. Lian, J. Hu, S. Zhuikov, Ag functionalized molybdenum disulfide hybrid nanostructures for selective and sensitive amperometric hydrogen peroxide detection, *Int. J. Electrochem. Sci.* 12 (2017) 8751–8776, <https://doi.org/10.20964/2017.09.69>.
- [41] E. Kurowska-Tabor, M. Jaskula, G.D. Sulka, Sensitive Amperometric sensing of hydrogen peroxide using Ag nanowire array electrode, *Electroanalysis* 27 (2015) 1968–1978, <https://doi.org/10.1002/elan.201400741>.
- [42] M. Yang, D.S. Kim, J.H. Yoon, S.B. Hong, S.W. Jeong, D.E. Yoo, T.J. Lee, S.J. Lee, K.G. Lee, B.G. Choi, Nanopillar films with polyoxometalate-doped polyaniline for electrochemical detection of hydrogen peroxide, *Analyst* 141 (2016) 1319–1324, <https://doi.org/10.1039/C5AN02134K>.
- [43] S. Mutyal, J. Kinsly, G.V.R. Sharma, S. Chinnathambi, M. Jayaraman, Non-enzymatic electrochemical hydrogen peroxide detection using MoS_2 -interconnected porous carbon heterostructure, *J. Electroanal. Chem.* 823 (2018) 429–436, <https://doi.org/10.1016/j.jelechem.2018.06.038>.